SANDIA REPORT

SAND2013-2716
Unlimited Release
April 2013

An Experimental Platform for Generating Richtmyer-Meshkov Instabilities on Z

Eric Harding and Matt Martin

Prepared by
Sandia National Laboratories
Albuquerque, New Mexico 87185 and Livermore, California 94550

Sandia National Laboratories is a multi-program laboratory managed and operated by Sandia Corporation, a wholly owned subsidiary of Lockheed Martin Corporation, for the U.S. Department of Energy's National Nuclear Security Administration under contract DE-AC04-94AL85000.

Issued by Sandia National Laboratories, operated for the United States Department of Energy by Sandia Corporation.

Available to DOE and DOE contractors from
U.S. Department of Energy
Office of Scientific and Technical Information
P.O. Box 62
Oak Ridge, TN 37831

Telephone: (865) 576-8401
Facsimile: (865) 576-5728
E-Mail: reports@adonis.osti.gov
Online ordering: http://www.osti.gov/bridge

Available to the public from
U.S. Department of Commerce
National Technical Information Service
5285 Port Royal Rd.
Springfield, VA 22161

Telephone: (800) 553-6847
Facsimile: (703) 605-6900
E-Mail: orders@ntis.fedworld.gov
Online order: http://www.ntis.gov/help/ordermethods.asp?loc=7-4-0#online

SAND2013-2716
Unlimited Release
April 2013

An Experimental Platform for Generating Richtmyer-Meshkov Instabilities on Z

Eric Harding
High Energy Density Experiments Department
Sandia National Laboratories
P.O. Box 5800
Albuquerque, New Mexico 87185-MS1193

Matt Martin
High Energy Density Physics Theory Department
Sandia National Laboratories
P.O. Box 5800
Albuquerque, New Mexico 87185-MS1189

Abstract

The Richtmyer-Meshkov (RM) instability results when a shock wave crosses a rippled interface between two different materials. The shock deposited vorticity causes the ripples to grow into long spikes. Ultimately this process encourages mixing in many warm dense matter and plasma flows of interest. However, generating pure RM instabilities from initially solid targets is difficult because long-lived, steady shocks are required. As a result only a few relevant experiments exist, and current theoretical understanding is limited. Here we propose using a flyer-plate driven target to generate RM instabilities with the Z machine. The target consists of a Be impact layer with sinusoidal perturbations and is followed by a low-density carbon foam. Simulation results show that the RM instability grows for 60 ns before release waves reach the perturbation. This long drive time makes Z uniquely suited for generating the high-quality data that is needed by the community.

ACKNOWLEDGMENTS

The authors thank Sasha Velikovich of the Naval Research Lab for many useful technical discussions and his continued encouragement of this project.

CONTENTS

FIGURES

TABLES

NOMENCLATURE

1D	One-dimensional
2D	Two-dimensional
EOS	Equation-of-State
ALEGRA	Arbitrary Lagrangian-Eulerian Multi-material Multi-physics Code
Hyades	Lagrangian Radiation Hydrodynamics Code
HED	High Energy Density
RM	Richtmyer-Meshkov
RT	Rayleigh-Taylor
KH	Kelvin-Helmholtz
CRF	Carbonized-Resorcinol-Formaldehyde
WDM	Warm Dense Matter
SNL	Sandia National Laboratories
ICF	Inertial Confinement Fusion
MagLIF	Magnetized Liner Inertial Fusion
NIF	National Ignition Facility
HE	High Explosivess

This page intentionally left blank.

1. INTRODUCTION

1.1. Hydrodynamic Instabilities

In many high-energy-density (HED) plasma systems the mixing of two or more materials is initiated by a shock wave propagating across an interface. Here we take mixing as a general term to describe the interpenetration of two materials existing in phases that range from plasma to solid. Many laboratory fusion type plasmas as well as astrophysical plasmas are subject to shock induced mixing. In particular, the inertial confinement fusion (ICF) community cares about hot ablator plasma mixing with the cold, internal fuel of a capsule causing decrease fusion yield. In any ICF concept, including the MagLIF concept being pursued on the Z accelerator[1, 2], the mechanical integrity of the confinement layer (i.e., the pusher) is important. There are three main instabilities that can initiate mixing, they are the following: Rayleigh-Taylor (RT), Richtmyer-Meshkov (RM), and Kelvin-Helmholtz (KH). The behavior of all three instabilities can be modified by the presence of magnetic fields and elastic-plastic effects. In this report, magnetic field effects are not discussed. We will concern ourselves here with two regimes, and these are the pure fluid regime in which the fluid has no resistance to deformation, and the elastic-plastic regime where the growth of the instabilities is modified by the yield strengths of the materials. Both regimes are important in HED plasmas. Furthermore, both the linear and non-linear development of the instabilities deserves attention, as well as the transition to turbulence. It should be pointed out that there are no experiments that have observed the complete evolution of a well-resolved, linear perturbation from initial growth to a fully turbulent state.

The intent of this report is to document the current theoretical understanding of the RM instability, and then discuss possible target designs for the Z accelerator. RM was chosen because there are fewer existing HED experiments for this instability. This fact is due to the difficulty in generating the instability compared to the RT instability. There are perhaps even fewer KH experiments, but there was not enough time to review and discuss the KH instability. Several relevant KH experimental papers are referenced here.[3-6] As will be shown later, the Z machine is capability of producing benchmark quality RM data that has not previously been available. This data is needed to bench mark both RM theories and numerical simulations. Z may also be capable of producing RM in a cylindrically imploding geometry for which there is currently no theoretical understanding.

1.2. Richtmyer-Meshkov Instability

The RM instability results when a shock wave crosses a perturbed interface that is composed of materials with different densities.[7, 8] Although, it has been shown that the instability may still exist if the density contrast is zero we will assume a density difference is required in order to understand the basic development of the instability.[9] See Figure 1.1 for a cartoon of the essential geometry. When the shock is in the process of crossing the individual perturbations the wave front becomes distorted due to the difference in shock speed between the two materials that make up the interface. The change in shock speed causes the shock front to change direction upon entering the second material (i.e., refract like an optical wave front propagating from atmosphere into a lens). The direction of the post-shock flow also changes direction in order to follow the

propagation direction of the shock. Therefore, the post-shock flow has different flow directions in each material. This results in a velocity shear that results in the perturbation growth. This shear flow exists on both sides of the perturbation. The shear flow is the driving force that causes the perturbation to grow. The shear flow can be characterized as a vorticity that instantaneously deposited on the interface. The vorticity rotates in opposite directions on opposing sides of the perturbation. The shear flow and vorticity interpretations are the equivalent. Most of the literature describes RM using the vorticity interpretation.

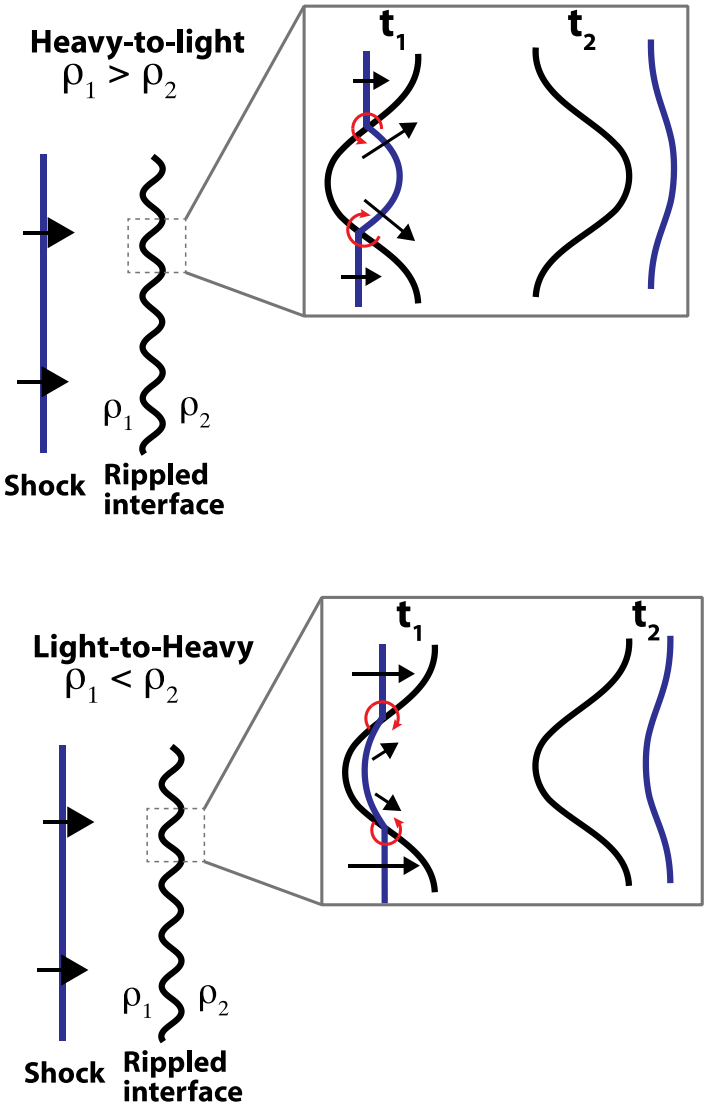

Figure 1.1. This illustration shows how the Richtmyer-Meshkov instability develops in cases where a shock traverse a rippled interface, going from high density to low density (top panel) and going from low-density to high-density (bottom panel).

In any case, the RM instability is not an instability in the sense that there is a feedback mechanism that continually amplifies the growth of a perturbation. It is merely an impulsive acceleration of an interface that launches the surface perturbations. As will be shown, the initial RM growth rate of a modest perturbation is linear, unlike the RT and KH growth rates, which are exponential. However, for the purpose of this document we will continue to refer to the RM phenomena as an instability in order to maintain continuity with the published literature. The RM instability produces features that are universal known as spikes and bubbles. A spike refers to the dense feature that is launched from the shocked interface, while the bubble is its less dense counterpart that projects in the opposite direction. The growth rate and morphology of the spikes and bubbles are the primary focus of RM research.

1.3. Linear Richtmyer-Meshkov Growth Rates

Richtmyer first proposed an impulsive model in which the perturbation is given a constant velocity after the passage of the shock wave.[7] The amplitude velocity is given by,

$$\dot{h}_{RM} = h_o k A^+ u_i \tag{1.1}$$

where η_o is the initial (unshocked) perturbation amplitude, k is the perturbation wavenumber ($\lambda/2\pi$), u_i is the interface velocity acquired after the passage of the shock, and A^+ is the post-shock Atwood number defined by,

$$A^+ = \frac{r_2^+ - r_1^+}{r_2^+ + r_1^+} \tag{1.2}$$

where the shock passes from material 1 with post-shock density ρ_1^+ to material 2 with post-shock density ρ_2^+. In this equation it is assumed that $\eta_o/\lambda < 0.1$. Once the amplitude grows beyond this value then linear theory of any kind is invalid. The above equation should be modified based on the sign of A^+. For $A^+ > 0$ (light to heavy), Richtmyer found better agreement if η_o was set to the post-shock amplitude η_o^+. The post-shock amplitude is given by,

$$h_o^+ = h_o \left(1 - \frac{u_i}{u_{shk}}\right) \tag{1.3}$$

where u_{shk} is the incident shock velocity in material 1. For $A^+ < 0$ (heavy to light), Meyer and Blewett[10] showed that better agreement was found if η_o was set to average amplitude $\eta_{o,ave}$ where

$$h_o^{ave} = \frac{1}{2}(h_o + h_o^+). \tag{1.4}$$

The previous equations for the perturbation velocity are referred to as the impulsive formulations. While these can be useful due to their simplicity, they lack much of the underlying physical processes that drive the perturbation growth. In particular, in highly compressible systems (i.e., those with high shock Mach numbers) the post-shock velocity field must be computed in order to correctly capture the linear evolution of the perturbation. Fortunately, linear analytic theories exist and have been develop by Velikovich[9] and Wouchuk[11, 12] independently. Both theories assume gamma law equations of state (EOS) for the interface materials. It may be possible to develop an analytic theory using the Mie-Gruneisen equation of state, but as of this writing the theory has not been published. This is currently an active area of research.[13]

In general the theories are divided into two classes depending on the Atwood number. For positive Atwood numbers the incident shock travels from a low-density material to a higher density material. This case is often referred to as the "light-to-heavy" problem. Here the incident shock generates a forward transmitted shock and a backward reflected shock. For negative Atwood numbers, known as the "heavy-to-light" problem, a forward transmitted shock is also produced, but the reflected wave is a rarefaction. The analytic solution of the heavy-to-light problem is more difficult due to the reflected rarefaction, which produces varying densities and pressures. Analytical linear theories have been developed for both light-to-heavy and heavy-to-light problems. Velikovich developed theories based on the shock generated velocity fields and Wouchuk has developed theories based on the vorticity fields.[9, 11, 12] Both interpretations yield identical results.

1.3.1. Non-Linear RM Growth Rates

There is less theoretical certainty in the non-linear regime. Here the perturbation amplitude is comparable to the wavelength. A transition to the non-linear regime roughly occurs when $k\eta > 1$ where k is the perturbation wavenumber. In the non-linear regime there are no exact analytic theories. However, there are several empirical models for the growth rate that attempt to capture the transition from linear to non-linear growth. Dimonte and Ramaprabhu review several of these models and compare them to FLASH simulations.[14] The comparisons are done at low Mach number ($M \sim 1$) for $0.25 < A < 0.98$. Dimonte and Ramaprabhu formulated the following model for bubble and spike velocities, V_{bu} and V_{sp}, respectively,

$$V_{bu/sp} = V_o \frac{1 + \left(1 \mp |A|\right)\tau}{1 + C_{bu/sp}\tau + \left(1 \mp |A|\right)F_{bu/sp}\tau^2} \tag{1.5}$$

where,

$$C_{bu/sp} \equiv \frac{4.5 \pm |A| + (2 \mp |A|)|kh_o|}{4} \tag{1.6}$$

$$F_{bu/sp} = 1 \pm |A| \tag{1.7}$$

$$\tau = k|V_o|t \tag{1.8}$$

and V_o = the initial growth rate, A = post shock Atwood number, τ = scaled time, k = perturbation wavenumber, and h_o = compressed perturbation amplitude. Here the equations will restated using the notation that is consist with the notation that was defined initial in this report.

$$V_{bu/sp} = \dot{\eta}_o \frac{1 + (1 \mp |A^+|)\tau}{1 + C_{bu/sp}\tau + (1 \mp |A^+|)F_{bu/sp}\tau^2} \tag{1.9}$$

where,

$$C_{bu/sp} \equiv \frac{4.5 \pm |A^+| + (2 \mp |A^+|)|k\eta_o|}{4} \tag{1.10}$$

$$F_{bu/sp} = 1 \pm |A^+| \tag{1.11}$$

$$\tau = k|\dot{\eta}_o|t \tag{1.12}$$

It should be noted that initial growth rate may not be linear depending of the value of $k\eta_o$. In either case of linear or non-linear initial growth, the growth rate is time dependent. The time dependent, linear growth is of course described by the exact analytic theories mentioned above. The initial, non-linear growth can be approximated using the expansion technique of Velikovich and Dimonte.[15] This was done with the use of the symbolic numerical software, Maple. The equations Dimonte and Ramaprabhu are presented here because it may be most relative to the applications that will be presented later in this report.

Several other non-linear empirical models should be mentioned here. Mikaelian, Zhang-Sohn and Sadot *et. al*., all have proposed various models that are designed to capture the asymptotic growth rates expected from potential flow.[16-19] These models may work well late in time.

1.4. Laser Driven RM experiments

Producing a long-lived RM instability in HED plasma is difficult because the lifetime of the instability is roughly equal to the duration of the driving source of energy. In the HED regime

this is typically a laser, a laser driven hohlraum, or a high velocity projectile. The Omega EP laser can provide a 30 ns laser pulse by stacking 3 individual pulses each with a 10 ns duration. There is a 4th beam that could be used to create a 40 ns drive, but this beam is usually needed for creating diagnostic x-rays that image the target. The 30 ns drive is currently the longest drive that has been demonstrated by any laser. An RM experiment has already been designed to use this capability.[20] Laser driven hohlraums offer no additional advantage since the length of the generated x-ray pulse is roughly equal to laser pulse length. High velocity projectiles will be discussed in more detail later in this report. It is also important to point out that high explosives (HE) have been used to generate RM instabilities and other hydrodynamic instabilities. However, the pressures generated by the HE are typically on the order of 0.1 Mbar. These relatively low pressures are comparable to the yield strength in many metals under high strain rates. Thus, HE may be used to examine the RM perturbation growth in a regime where a material will resist the deformation resulting from the instability.

Lasers were the energy source for all previous RM experiments performed in the HED regime. Dimonte *et. al*. performed heavy-to-light experiments using a hohlraum driven by a 3 ns pulse from the NOVA laser.[21, 22] Here η_o = 10 μm and λ = 100 μm. Thus, the experiment started on the edge of the non-linear regime. Simulations indicated that the interface experienced a steady drive for 2-3 ns. The target consisted of a Be/foam interface (ρ_1 = 1.7 g/cc and ρ_2 =0.12 g/cc, A^+ = -0.67) that was driven by a M ~ 10 shock. The Be piece was formed by vapor plating Be onto a Cu mandrel with a machined perturbation. The quoted density is lower than bulk Be due to the deposition process. The foam was a mixture of a CH_2O matrix called AGAR and an x-ray dopant Na_2WO_4. As shown by Holmes et. al. and Dimonte and Ramaprabhu the models and numerical simulations do not fit the data well.[14, 23] No explanation is given for the discrepancies. The data consists of amplitude measurements taken by side-on and face-on radiographs. The small amplitude, early time measurements used the face-on radiograph, while the side-on radiograph measured the larger amplitudes that appeared later in time. The interface experienced a 1 eV preheat. It is not clear how the preheat affected the perturbation growth and amplitude measurements.

Another laser experiment was published by Glendenning *et. al.* using the Omega laser. Similar to the Dimonte *et. al*. NOVA experiments, Glendenning *et. al.* performed a heavy-to-light experiment.[24] Three sets of beams, each with duration of 3.7 ns, were stacked in time to give a 11.1 ns drive. The perturbed interface is composed of polycarbonate (1.2 g/cc) with an embedded CHBr tracer strip (ρ_1 = 1.23 g/cc) and CRF foam (ρ_2 = 0.1 g/cc). The perturbation is described by λ = 150 μm and η_o = 7 or 22 μm. The laser first strikes a 20 μm thick polycarbonate layer and transmits a shock into a 170 μm CHBr layer that is intended to block preheat x-rays from reaching the perturbed interface. The shock is then transmitted into the 50 μm thick polycarbonate/CHBr layer and reaches M ~ 10. This yields A^+~ 0.5. The average interface velocity as measured from a streaked image of a flat interface is 22 ± 1 μm/ns over the length of the experiment. The perturbation inverted its phase and started to grow at ~11 ns and reached ~ 40 μm in amplitude by 24 ns. The paper argues that the small decrease in the interface velocity introduced a 5% Rayleigh-Taylor growth component over the duration of the experiment. Simulations suggested the x-ray preheat of the interface is less than 0.1 eV due to the insulation provided by brominated plastic layer. The error bars on the data are plus/minus 2-

3 μm. This is surprising considering the data was obtained with a framing camera that used 10 μm pinholes. No explanation is presented concerning how the error bars were computed.

Yefim *et. al.* have carried numerous RM experiments using the Nike laser. They have conducted experiments to examine ablative RM, feedout, classical RM, impulsive loading, and re-shock.[25, 26] All of these experiments have recorded a continuous time history of the lateral redistribution of the perturbation mass using a monochromatic spherical crystal imager in a face-on geometry coupled to a streak camera. The Nike laser delivers a 4 ns pulse to the target with a 400 μm spot size. The targets typically used λ = 30 to 45 μm with η_o equal to several microns. Due to the high contrast provided by the monochromatic imager, the mass variations and oscillations are measured with high accuracy. Recently Yefim *et. al.* measured the time evolution of a shocked plastic/vacuum (A^+ = -1) interface using side-on radiography.[27] Here a new stroboscopic backlighter technique with two sequential x-ray pulses was used to capture the evolution on a single piece of image plate. The targets had perturbations with λ = 46 μm and η_o = 7.5 μm ($k\eta_o$ = 1.0) on the rear side of a 53 μm thick polystyrene foil.

The dimensions of all the laser experiments discussed above were limited by the laser spot size. The spot size is around 1 mm or less for Omega, Nike, and NOVA. The National Ignition Facility (NIF) at Lawrence Livermore National Laboratory will be able to provide larger laser spots. Larger scale hydrodynamic instability experiments have been proposed for NIF, yet none have been performed so far. RM experiments have been performed with energy sources other than lasers. These will be discussed in the next section.

1.5. RM with Shock Tubes, Drop Tanks, and High-Explosives

Here we will briefly discuss RM experiments carried out with shock tubes, drop tanks, or high-explosives (HE). The intent here is not to provide an exhaustive list, but to discuss the most notable experiments.

1.5.1. RM in Shock Tubes

Shock tube experiments produce shock waves by puncturing a reservoir of pressurized gas at one end of a gas filled tube. The challenge in these experiments is to create a well-defined sinusoidal interface between two gases that does not interfere with the hydrodynamics of the RM instability. The light-to-heavy experiments of Sadot *et. al.* used a 0.1 μm nitrocelluloid membrane stretched over thin copper wires to create a interface between Air and SF_6 (A = 0.67).[19] A shock with M ~ 1.3 is generated in Air and then passed into SF_6. Single-mode experiments were carried out with λ = 16, 26, 40, and 80 with η_o = 2 mm. A similar experiment was conducted by Aleshin *et. al.* using Xe and Ar gases (A = 0.53) with M ~ 3.5 and λ = 36 mm .[28] In both experiments, imaging of the perturbation was done using a schlieren technique. More recently, work has been done to generate sinusoidal interfaces without membranes. The work published by Jacobs and Krivets used a vertically suspended shock tube that is gently rocked back and forth by a stepper motor in order to set up a standing wave inside the tube.[29] Similar to Sadot *et. al.*, a shock with M ~ 1.3 is passed from Air (mixed with acetone vapor) to SF_6 (A^+ = 0.664). Two sets of single mode experiments were performed. One with λ = 59.3 mm and η_o = 2.90 mm and another with λ = 35.5 mm and η_o = 1.47 mm. A planar laser induced fluorescence

(PLIF) technique is used to image the perturbation growth. A thin laser sheet was propagated down the axis of the shock tube. The laser causes the acetone to fluorescence, and the visible emission is recorded by a charge-coupled device (CCD). The low repetition rate of the laser required a new experiment for each desired time. Nevertheless, the image quality is remarkable. Data was recorded from $\tau = 0$ to 10, thus capturing linear to deep non-linear growth. Overall, this data best agrees with the model of Sadot *et. al.*.

1.5.2. Incompressible RM with a Drop Tank

Niederhaus and Jacobs developed an apparatus to study incompressible RM in liquids.[30] In their setup a Plexiglas tank is filled with light and heavy liquids and then gently oscillated in order to create a standing wave that serves as the initial perturbation for the RM instability. The light fluid is water/isopropanol mixture and the heavy fluid is a water/calcium nitrate solution. The fluids are miscible so the surface tension was expected to be negligible. Both single and multi-mode experiments were conducted. The single mode experiments had $\lambda = 82.6$ mm and $\eta_o = 3.0$ mm ($k\eta_o = 0.23$). The tank is dropped from a 3 meter tall vertical tower. The tank impacts a spring that provides a 50 g impulsive acceleration imparted over 26 milliseconds. After the bounce the spring was retracted and the tank free fell in a micro-gravity environment. During free fall the RM instability is allowed to evolve without experiencing any further accelerations. The flow evolves up to ~900 milliseconds ($\tau \sim 30$) and $k\eta^+ \sim 4$ for the single mode experiment. PLIF and a CCD camera were used to visualize the flow. The RM instability developed from the linear and into the deep non-linear regime. The images are of remarkable quality. It is interesting to note that a shockwave was not generated in this experiment, and thus the experiment was entirely incompressible.

1.5.3. RM with High-Explosives

High-Explosives (HE) can be used to drive shockwaves across perturbed interfaces formed by solid materials. Two examples of this are referenced here.[31, 32] Typical HE experiments generate pressures on the order of 0.1 Mbar. Recent experiments from Dimonte *et. al.* and Buttler *et. al.* investigated RM instabilities formed at a perturbed metal/vacuum interface that was driven by HE launched shocks.[33, 34] The post-shock pressures were between 0.22 to 0.36 Mbar. These experiments explored ejecta that formed at the rear (vacuum side) of the solid Cu and Sn plates when the shock broke out through the perturbation and into vacuum. Perturbations on the rear of the pates had $\lambda \sim 550$ μm with $\eta_o = 22$ to 175 μm ($k\eta_o = 0.25$ to 2). These perturbations provided the seeds for the RM instability. In the region of the RM spikes the metals experienced high-strains rates (10^7 s^{-1}) and high strains (700%) as a result of the elongation. The growing perturbations were imaged with the proton radiograph at the pRad facility. The spatial resolution was ~ 80 μm and temporal resolution was ~ 200 ns. In the Cu experiment with $k\eta_o = 0.12$ no RM spike growth was observed, but in the $k\eta_o = 0.35$ case spike growth and arrest was observed. For these cases the spikes and bubbles are not resolved by pRad imaging. The observation resulted from laser Doppler velocimetry (LDV) measurements. The lack of, or reduction, in RM growth was attributed to the high flow stress that resulted from the rapid elongation of the material in the RM spikes. Overall, HE driven experiments produce unsupported shocks, which makes it difficult to generate a pure RM instability.

1.5.4. Needed Future RM Experiments

The RM instability in solid materials is of greatest here. As was mentioned above, only lasers and HE have accessed the solid regime, and there exist only a few HED experiments. Furthermore, both types of experiments have produced low-resolution images that do not reveal the details of the initial growth of the perturbations. There remain several areas of RM research that deserve further experimental investigation.

1.5.4.1. Classical RM growth

A classical experiment should have a moderate Atwood number ($A^- < 0.9$) and investigate the transition from linear to non-linear growth in an HED plasma that behaves as a fluid, with no strength affects. This type of experiment would start with $k\eta_o < 1$ and then track the perturbation to $k\eta_o \sim 10$ or larger. In previous experiments this has been difficult due to the short temporal duration of the driver. It would be desirable if this experiment could vary the shock Mach number from M~1 to 2, to M > 10. In this way, compressibility effects could be investigated. As the Mach number increases, the compressibility effects should persist later in time as the perturbation continues to grow from the linear to non-linear regime. This type of experiment could be used to benchmark and discriminate between the many different empirical theories in the HED regime.

1.5.4.2. Ejecta formation

Here it would be interesting to track the early time formation of the ejecta spikes for an initial perturbation with $k\eta_o > 1$ at a metal/vacuum interface ($A^- = -1$). The shock Mach number should be varied from M ~ 1, so that the material's yield strength can affect the growth, to M >>1 so that strength effects are negligible. The material type and initial perturbation (λ and η_o) can also be varied in order to test current strength theories of Piriz *et. al.*. Using RM theory to describe ejecta formation is just one approach that must be verified with experimental data.

1.5.4.3. Bubble merger

The bubbles formed in a multi-mode interface grow at different rates and eventually combine to form larger bubbles. The time scale on which the bubbles merge in the HED regime has not been measured experimentally.

1.5.4.4. Turbulent Transition of Spike Tips

Deep into the non-liner regime the spike tips begin break up as the surrounding flow becomes turbulent. This has not been observed in the HED regime due to limited diagnostic resolution and the short drive times available in the experiments. Understanding the transition is important for developing mix models for material interfaces. Currently it is not clear if isotropic turbulence will result from a long-lived RM instability.

1.5.4.5. Converging Geometries

So far, only planar geometries have been discussed. It would also be interesting to investigate RM in a cylindrically converging geometry. Cylindrical liners are routinely fielded on Z, so only minor modifications would need to be made to an existing target. This is discussed further later in the report. Here it is important to note that no analytic theory exists for RM growth rates in converging geometries.

2. DESIGN OF A RICHTMYER-MESHKOV EXPERIMENT FOR Z

The Z-machine is a large voltage generator that can provide up to 27 MA in 100 to 300 ns. This enormous current is typically used to implode wire arrays or cylindrical tubes known as "liners". It can also be used to drive currents, in opposite directions, along two parallel metal plates. When this occurs the large magnetic pressure between the plates causes them to explode outward. One plate is typically much more massive than the other so that only one is launched with a high velocity. This high velocity plate is known as a "flyer plate." Flyer plates are used to drive shocks or isentropic compression waves into various materials of interest. Typical flyer plate velocities range from 16 km/s up to 32 km/s for coaxial load designs. A more aggressive strip-line design can push the flyer velocity up to 40 km/s. Drake suggested that flyer plates could be used as a driver to generate long-lived hydrodynamic instabilities.[35] Figure 2.1 illustrates the basic setup for a Z experiment.

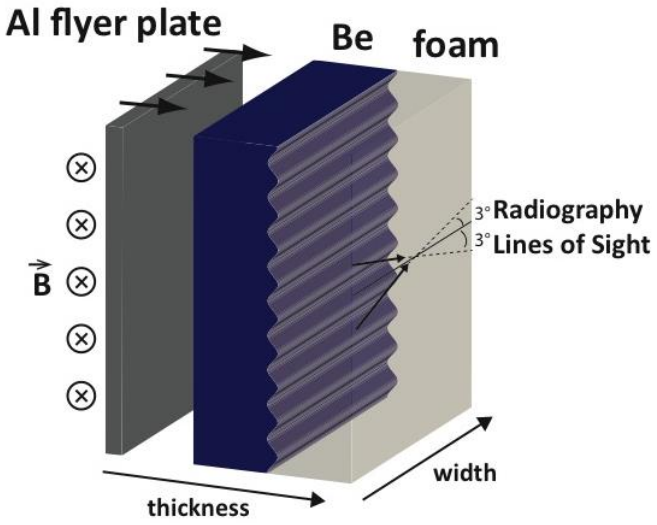

Figure 2.1. Shown here is the conceptual target design for a heavy-to-light RM experiment driven by a flyer plate. An Al flyer plate impacts Be with a rippled rear surface.

Flyer plates offer several advantages compared to lasers. First, the flyer plate dimensions are on the order of centimeters, which are much larger then the millimeter spot size of most lasers. This allows the use of a larger target and hence larger initial perturbations. These large perturbations are easier to resolve with imaging diagnostics. Second, flyer plates can maintain a steady shock much longer than any laser pulse demonstrated so far. As will be shown in a later section, simulations indicate that a flyer plate experiment could maintain a steady shock for 90 ns in a RM relevant target. Finally, flyer plates do not generate high-energy radiation or electrons that run ahead of the shock and preheat the perturbed interface. Therefore, the initial interface conditions and the shock Mach numbers are clearly defined. The disadvantage of flyer plates is that they cannot generate pressures as large as those generated with lasers. Nevertheless, flyer plates can access pressures and densities that are of interest to warm dense matter physics, and so their advantages make them an attractive option for generating instabilities. The primary purpose of this section is to develop a design for a classical RM experimental as described in Section 1.5.4.1.

2.1. Classical RM Experiment

The classical RM experiment presented here will use an existing flyer plate design. This design is the same as that used for the recent X-ray Thomson Scattering experiments performed on Z. The setup has been optimized to generate a long-lived steady shock, and is thus well suited for an RM type experiment. The details of the flyer setup are presented in Table 2.1.

Table 2.1. Listed here are the characteristics of a particular flyer plate configuration that will be used for the RM target design proposed in this report. This configuration was previously shot on the Z-machine.

Flyer Material	**Al 6061-T6, 2.7 g/cc**
Initial Flyer Thickness	**1.2 mm**
Thickness at Impact (T < 933 K)	**0.450 mm**
Flyer Velocity at Impact	**16.7 km/s**
Z Charge Voltage	**53.6 kV**
Flight Gap	**4 mm**
Cathode Size	**9 x 2 mm**

Currently on Z, radiography is performed with a spherical crystal imager that uses either a Si He-α (1.86 keV) x-ray backlighter or a Mn He-α (6.151 keV) x-ray backlighter.[36, 37] The imager provides two radiographs separated by an arbitrary delay that cannot exceed 20 ns. Both images are taken from line of sights that are offset by 3° with respect to the horizontal plane in which the flyer plate propagates. One radiograph views the target at +3° and the other views it at -3°. Relevant data concerning the operation the spherical imager is presented in Table 2.2.

Table 2.2. Listed here are the specifications for the spherical crystal imager. Two crystals are used to provide two separate radiographs (known as "frames") spaced in time.

X-ray Energy	**6.151 keV**
Magnification	**6x**
Field of View	**10 x 4 mm**
Spatial Resolution	**15 μm**
Min. Detectable Transmission Variation	**6%**
Collection Time	**1 ns**
Max. Frame Separation	**20 ns**
Detector Type	**Fuji Image Plate**

Due to the limited penetration depth of 1.86 keV x-rays, our target design will only consider the 6.151 keV backlighter. This immediately places limitations on the thickness and material types

that can be used in the target. In general the target will consist of two materials. See Figure 2.1 for a schematic drawing of an idealized target. The first material will be the impact layer. This is the slab of material that is first impacted by the flyer plate. On the rear side (side opposite the flyer) a single mode, 2-dimensional perturbation is present. Behind the impact layer is another material that completes the interface. Ideally, the second material will have a matching perturbation so that no voids are present at the contact surface.

To continue further, the experimental design requirements are specified to allow for optimization within the following constraints.

1. The experiment will be a heavy-to-light design where the impact layer will have a higher density than the second material. This means, $\rho_2 < \rho_1$ (i.e., $A^- < 0$).
2. The shock location and planarity will be resolvable with radiography on both sides of the interface. This is necessary so that the interaction of the shock with the perturbation can be directly observed.
3. Two separate radiographs will be taken to observe the time evolution of the perturbations. By invoking this requirement we are forced to deal with the 3° rotation of the lines-of-sight. It is important to note that if only a single image at one time was required, the 3° rotation would not be an issue. In this case, the line-of-sight is 0° and the field-of-view is increased since a single, large spherical crystal is used instead of two smaller ones.
4. The target will allow for the observation of both linear and non-linear growth in a single shot. The initial perturbation will be sinusoidal. It will have $\eta_o/\lambda \sim 0.05$ and be observable in pre-shot radiographs.
5. The lateral rarefaction waves will not disturb more than 20% of the total target width at the time of observation.

2.1.1. Target Material Selection

Requirements one and two will guide our thinking toward which materials are acceptable. It is known from previous Z experiments that it is possible to maintain steady shocks for many 10's of nanoseconds, and possibly up to 100 ns. If a modest sound speed of 10 μm/ns is assumed for the post-shock state of the second material, around 1 mm of the target on each side could be disturbed by the lateral rarefaction wave that propagates inwards in the target. Thus, the target must be many millimeters wide so that the entire width of the target is not consumed by the lateral rarefactions. This is quite thick considering the target must be diagnosable with 6 keV x-rays. There two approaches to this problem. One, the target is made thick enough such that the disturbed portions of the target remain relatively small compared to the total target width. This approach will require the use of materials with low opacities at 6 keV. Two, the materials have a thin undisturbed portion that may be thinner than the disturbed portions, but the undisturbed portion contains a localized, high-Z trace element that concentrates all of the opacity in the undisturbed portion. The second option is the one most frequently used for laser experiments. The issue is that the trace element must be embedded in a material that has the same density and compressibility as the surrounding material so that it has similar hydrodynamic behavior. This is most easily accomplished in plastics such as polystyrene, which can be doped with a few percent Bromine or Iodine. The doping increases the density to 1.4 g/cc, which is similar to the density of polyimide. Thus the doped polystyrene, known as a tracer layer, can be easily embedded in

polyimide. This technique was used in many previous laser driven hydrodynamic experiments on the Omega laser. At the time of this writing, it appears that plastics and foams are the only viable options for creating tracer layers. Doping low-Z metals such as Li or Be with trace high-Z elements does not appear to be a viable option. Because the target must be several millimeters wide, plastics are too opaque to serve as an impact layer. The best option is Be. And low-density foam appears to be the best option for the second material. Thus, the target will be composed of a Be impact layer followed by a low-density (0.05 to 0.1 g/cc) foam. Here we propose using carbonized-resorcinol-formaldehyde (CRF) foam due to its machinability and small cell size ($<< 1$ μm).

It has been suggested that a few microns of Au could be inserted into the Be and used as a tracer layer. The idea is to section the Be and coat one of the freshly machined surfaces with Au using vapor deposition. The Be would then be reassembled under slight clamping pressure and glued around the edges. A final machining process would then cut the perturbations. Due the relatively thin coating of Au compared to the width of the Be, the Au might not disturb the hydrodynamics. Two-dimensional simulations will be needed to investigate this idea further.

2.1.2. Impact Layer Optimization

In order to maximize the duration of the steady state shock conditions, Drake derived a equation for the impact layer thickness assuming a gamma law equation of state for all materials.[35] The impact layer thickness must be related to the flyer thickness through the following equation,

$$\frac{d_I}{d_F} = \sqrt{\frac{r_F}{r_I}}\sqrt{\frac{g_F+1}{g_I+1}}\frac{[2/(g_F+1)+\sqrt{2/(g_F(g_F-1))}]}{[2/(g_I+1)+\sqrt{2/(g_I(g_I-1))}]} \tag{2.1}$$

where d_I is the thickness of the impact layer, d_F is the thickness of the flyer plate at the time of impact, ρ_I is the density of the impact layer, ρ_F is the density of the flyer plate at impact, and γ_I and γ_F are the polytropic indexes of the impact layer and flyer, respectively. This equation assumes that the steady shock duration is maximized when the flyer and impact layer rarefactions arrive simultaneously at the flyer/impact layer contact surface. Taking $\gamma_F = \gamma_I = 5/3$, $\rho_F = 2.7$ g/cc, $\rho_I = 1.85$ g/cc, and $d_F = 0.45$ mm, gives $d_I = 0.544$ mm. Notice when $\gamma_F = \gamma_I$ the equation depends only on the densities.

2.1.3. One-Dimensional Simulations with Hyades

One-dimensional (1D) simulations were carried out using the Lagrangian, radiation hydrodynamics code Hyades.[38] An Al flyer with a thickness of 0.45 mm was launched at 16.7 km/s into a Be impact layer. The initial Al flyer velocity was made constant, and the entire thickness of the flyer was initially solid density (2.7 g/cc) at impact. The Be was 0.544 mm thick and followed by carbon foam (0.05 or 0.1 g/cc). All materials used a polytropic index of 5/3. The shock arrives at the interface at 44 ns and then rarefaction arrives later at 130 ns. This yielded 86 ns during which the interface held a constant velocity. Due to the low pressure and low ionization achieved in the target materials, a gamma law EOS is most likely inaccurate. So, the same simulation was repeated, but this time SESAME EOS tables were used for Al (3718)

and Be (2020). A solid density polystyrene EOS table (SESAME 7592) was used for the foam. In this simulation the shock arrived at 29 ns, and later the rarefaction arrived at 87 ns. This yielded a shorter steady drive time of 58 ns. The important values from the simulations with the tabular equations of states are listed in **Table 2.3**. Because the reflected wave from the Be/foam interface is a rarefaction and not a shock, the Be density releases down to a value less then the shocked state. The release density depends on the initial foam density as shown in **Table 2.3**. Having a lower Be density at the interface is advantageous for this experiment because it increases the transmission of the backlighting x-rays. This may allow the radiography to capture the rarefaction traveling back into the shocked Be.

Table 2.3. Listed here are the output values from a 1D Hyades simulation using SESAME tabular equations of state. The initial flyer thickness and velocity were 0.45 mm and 16.7 km/s respectively. The Be impact layer was 0.544 mm thick and was followed by carbon foam. Values are shown for two foam densities.

Hyades	0.05 g/cc foam	0.1 g/cc foam
Shock in Be velocity	18.8 km/s	18.8 km/s
Interface velocity	17.1 km/s	16.5 km/s
Shocked Be density	3.6 g/cc	3.6 g/cc
Released Be density	1.9 g/cc	2.1 g/cc
Shocked Foam density	0.23 g/cc	0.4 g/cc
Shock Be pressure	3.1 Mbar	3.1 Mbar
Released Be pressure	0.2 Mbar	0.36 Mbar
Released Be sound speed	10 km/s	10.5 km/s
Shocked foam sound speed	11.5 km/s	12 km/s

Figure 2.2 below shows the output from the 1D Hyades simulation with the 0.050 g/cc foam. This simulation shows that the shock reaches the Be/foam at 29 ns. Later at 45 ns the flyer rarefaction and the Be rarefaction meet simultaneous at the flyer/Be contact surface. Then at 82 ns the rarefaction reaches back to the Be/foam. At this point the interface experiences a pressure gradient and begins to decelerate. The pure RM growth phase is over since the interface is now Rayleigh-Taylor unstable.

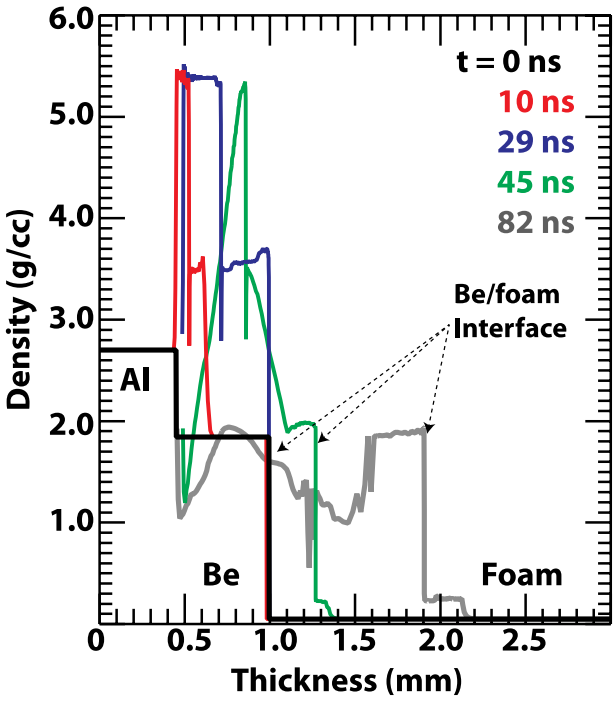

Figure 2.2. This plot shows the results of a 1D Hyades simulation using SESAME equations of state for Al, Be, and Foam.

2.1.4. One-Dimensional Simulations with LASLO

A more advanced 1D simulation was performed with the LASLO code.[39] In this case, an experimental current history produced by the Z-machine was used as the input to the code. The code then calculated the magnetic pressure generated by the current, and used the calculated magnetic pressure as the drive for the Al flyer plate. The code also calculated the melting of the rear surface of the flyer due to Ohmic heating. This is an important aspect of the simulation because the thickness of the remaining solid portion of the flyer largely determines the steady shock duration. Fortunately, this particular flyer configuration has already been optimized for a large solid thickness.

LASLO simulations used the following SESEAME EOS tables for the Al, Be, and Foam: 3700, 2020, and 7171 (POLYCH2) respectively. These simulations were coupled to the optimization software DAKOTA. The goal was to determine the Be thickness that would maximize the constant velocity time of the interface. Because Drake's assumption of a gamma law EOS was not accurate in this case, there was a need to verify that the derived flyer to impact layer thickness remained valid. For the current history assumed here, it was found that a Be thickness of 0.550 maximized the constant velocity time. At this thickness the constant velocity time was 90 ns**.** Table 2.4 lists the values the relevant values from the LASLO simulation. The LASLO values are similar to the Hyades results, except LASLO predicts a longer steady shock time.

Table 2.4. Listed here are the output values from current driven simulations using LASLO 1D with tabular equation of states. Values are shown for two different foam densities.

LASLO	0.05 g/cc foam	0.1 g/cc foam
Shock in Be velocity	18 km/s	18 km/s
Interface velocity	17.3 km/s	16.1 km/s
Shocked Be density	3.8 g/cc	3.8 g/cc
Released Be density	1.9 g/cc	2.1 g/cc
Shock Be pressure	3.2 Mbar	3.2 Mbar
Released Be pressure	0.26 Mbar	0.43 Mbar
Released Be sound speed	11.8 km/s	13.1 km/s
Shocked foam sound speed	11.9 km/s	11.8 km/s

2.1.5. Determination of the target thickness

The previous 1D calculations have optimized the material thicknesses. Here the "thickness" corresponds to the dimension that is along the flyer's plate's direction of travel. The term "width" will correspond to an orthogonal direction, and is along the line-of-sight of the radiograph. When determining the width of the target two parameters must be considered. One is the image contrast between the different regions (e.g., shocked and unshocked Be or Be and foam) of the target. And the other is the speed of the lateral release waves that propagate inward and disturb the growing perturbations.

In Figure 2.3 the transmission of various materials is plotted against the target width. This plot is important for determining the transmission difference between different target materials. As stated in the experimental requirements, the experiment must allow the planarity of the shock to be evaluated before it impacts the perturbation. To do this requires a minimum of 6% transmission difference between the shocked and unshocked Be. In this case the shocked Be can be completely opaque (0% transmission) while the unshocked Be must have a minimum transmission of 6%. As seen in
Figure 2.3 this occurs if the Be is 6.5 mm thick. The Figure allows shows that there is enough contrast between the unshocked Be and foam such that the initial perturbation should be visible if the perturbation is above the imaging resolution. After the shock crosses the interface and into the foam, the foam density increases by ~ 4x and the Be density decreases to between 1.9 to 2.1 g/cc depending on the initial foam density. As shown in Figure 2.3, there is no contrast between the released Be and the shocked foam if the shocked foam density is 0.4 g/cc (initial density = 0.1 g/cc). However, the contrast increases if the shocked density is 0.23 g/cc (initial density = 0.05 g/cc). Then the transmission difference between the released Be and the shocked foam is around 14% for a width of 0.65 mm. The transmission of the Be impact layer limits the width of the target. Both the shock in the Be as well as the post-shock Be/foam interface can be imaged with contrast differences greater than 6% if the target is 6.5 mm wide. The width could be less if more contrast was required. However, the effects of the lateral release waves must first be considered.

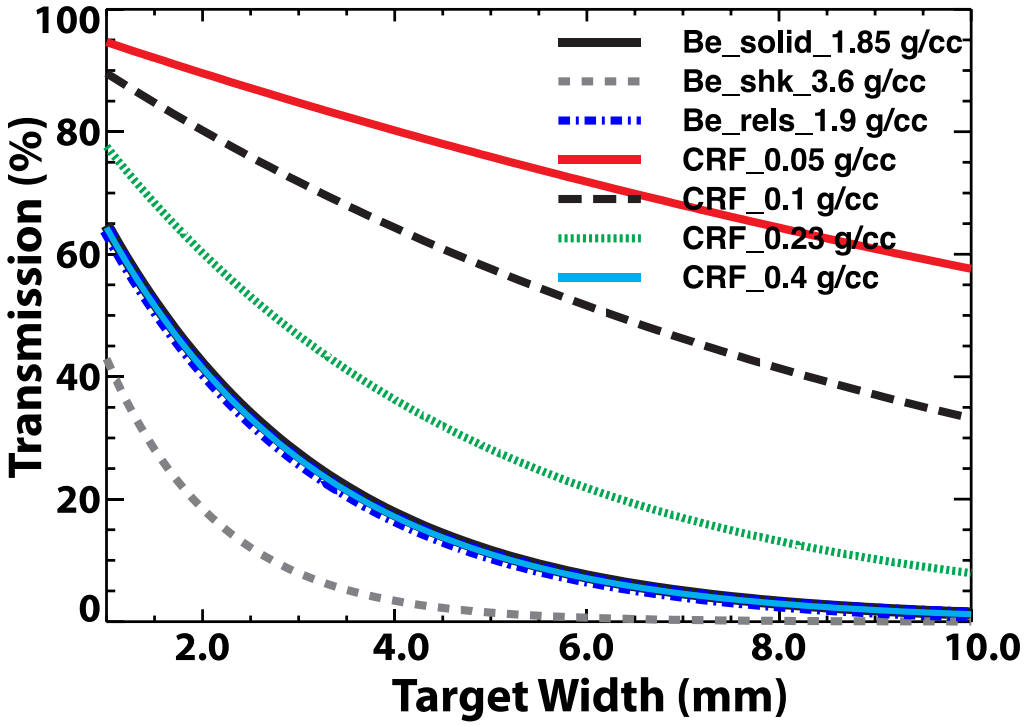

Figure 2.3. Plotted here is the transmission of various target materials as a function of target width for a backlighter energy equal to 6.151 keV. The Be curves are for ambient, shocked, and release states. The composition of CRF was assumed to be $C_{1000}O_{48}H_{65}$.

2.1.6. Lateral Release Waves

There are important edges effects that must be considered when determining the width of the target. Here the term "lateral" will refer to the two directions that are orthogonal to the flyer propagation direction. The target is surrounded by vacuum so when the shock reaches the edge of the target, the material (Be or foam in this case) releases into vacuum, which sends a rarefaction wave inward to the center of the target. The leading edge of the rarefaction travels at the local sound speed of the material. The low-density foot on the opposite end of the rarefaction travels into vacuum at a speed equal to a few times the bulk sound speed. As the rarefaction travels inward it will disturb the growing perturbations that are located near the edges of the target. As stated in the target requirements, less then 20% of the total width should be disturbed by the lateral rarefactions. The distance the rarefaction has travel into the target is equal to the product of the sound speed and the elapsed time since the shock crossed the interface. The maximum elapsed time is around 60 ns and the shocked foam sound speed is 12 km/s. Thus, 720 μm of foam is disturbed on each edge of the foam. If the foam is 6.5 mm wide, 22% of the width is disturbed by the rarefaction.

2.2. Initial Perturbation Selection

The wave timing, material types, and dimensions were determined in the preceding sections. This section is concerned with the selection of the initial interface perturbation. Depending the value of the perturbation $k\eta_o$ the growth can begin in a linear regime ($k\eta_o < 1$) or in a non-linear regime ($k\eta_o >> 1$). Ideally, a single experiment would span both regimes.

2.2.1. Meyer-Blewett Growth Rates

The Meyer-Blewett growth rate can be rewritten as follows,

$$\dot{h}_{MB} = kh_o\left(1 - \frac{u_i}{2u_{shk}}\right)A^+u_i, \tag{2.1}$$

where all variables were describe in Section 1.1.1. The term in parenthesis is an amplitude compression factor. In the previous sections it was determined that the materials would be Be and CRF foam (0.05 g/cc), and the 1D ALEGRA simulations give the values necessary to calculate the growth rate. Table 2.5 lists the values for u_i, u_{shk}, ρ_1^+, ρ_2^+, and A^+.

Table 2.5. Listed here are the values used for calculating the Meyer-Blewett RM growth rate for the proposed RM target.

u_i	**17.1 km/s**
u_{shk}	**19.0 km/s**
ρ_1^+	**1.9 g/cc**
ρ_2^+	**0.225 g/cc**
A^+	**-0.79**

The growth rate becomes $-7.4k\eta_o$ with units of km/s (μm/ns) and the time dependent growth is $-7.4k\eta_o t$ in units of km (μm). The negative sign means this is a heavy-to-light interface and thus the perturbations are inverted (i.e., troughs become spikes). For the amplitude to begin in the linear regime we propose setting $k\eta_o = 0.31$ or 0.63, which corresponds to 5 and 10% amplitude perturbations respectively. Using Equation 2.1 and the values in Table 2.5, the maximum growth after 60 ns is 139 μm and 280 μm for the 5% and 10% perturbations, respectively. It would also be interesting to try $k\eta_o > 1$, perhaps $k\eta_o = 6.3$. Currently, there are no analytical or semi-empirical theories that can predict the growth of such a large perturbation. The authors suspect that ejecta forms in these cases.

2.2.2. Perturbation wavelength selection

Next the perturbation wavelength must be selected. The 3° line of sight to the target imposes a significant constraint on the wavelength. Because of the angled line of sight the radiograph will not view directly down the rows of perturbations. In fact, if the wavelength is short enough the

peaks from two neighboring rows of the perturbations can eclipse and completely obscure the trough in between them. Assuming the rows of perturbations run the entire width of a 6.5 mm wide target, this will occur if $\lambda < 6.5\text{Tan}(3°) = 340$ μm. Here we will choose a wavelength that is twice this value, $\lambda = 680$ μm, which yields $\eta_o = 34$ μm and 68 μm for 5% and 10% perturbations respectively. After 60 ns of linear growth, the final amplitudes, given by η_{max}, are 173 μm ($k\eta_{max} = 1.6$) and 348 μm ($k\eta_{max} = 3.2$) for the 5% and 10% perturbations respectively. After the perturbation obtains $k\eta_o > 1$ the linear growth rate is no longer accurate. The non-linear growth has been shown to be slower than the linear growth, thus the values for η_{max} presented here represent an upper bound on the maximum amplitude.

Smaller wavelengths require that the perturbation does not run the entire width of the target. The perturbation could be machined into only the central portion of the Be, leaving a flat area between the perturbation and the edges of the target. To further evaluate this concept, two-dimension simulations will be required. The 3° viewing issues could also be eliminated if only one radiograph was required. In this case, a single crystal and backlighter are used to image the target directly along the rows of perturbations. The disadvantage of this approach is that only a single image, at one time would be obtained. This would prevent a growth rate measurement with only a single shot. The smallest resolvable amplitude is 15 μm, thus with a 5% perturbation yields $\lambda = 300$ μm. After 60 ns of growth $\eta_{max} = 154$ μm and $k\eta_{max} = 3.2$, which is two times more developed than the $\lambda = 680$ μm perturbation.

2.2.3. Summary of Design from 1D simulations

Table 2.6 summarizes the proposed 5% and 10% amplitude perturbations for a linear RM experiment on Z. The shock speed in the Be as predicted by the 1D simulations was 18.8 km/s, which gives a Mach number of 2.2 assuming a cold Be sound speed of 8.1 km/s.

Table 2.6. Listed here are the proposed perturbations for a linear RM experiment on Z that will capture two separate radiographs. The maximum amplitudes are calculated assuming a linear growth rate using 60 ns of growth time.

	5% Amp. Perturbation	10% Amp. Perturbation
λ	680 μm	680 μm
η_o	34 μm	68 μm
η_{max}	173 μm	348 μm
$k\eta_{max}$	1.6	3.2

2.3. Ejecta, Strength, and Other Experiments

Once the classical RM experiment proposed here has been successfully demonstrated, it will be relatively easy to adapt the design for other types of RM experiments. For example, if the foam was removed so that $A^+ = -1$ the experiment may produce ejecta. Furthermore, because of the unique current pulse shaping capabilities on Z, an isentropic compression wave can be produced in the Be impact layer. The yield strength of the Be would then affect the RM growth rate. Piriz *et. al.* developed a theory that determined the yield strength of the material based on the RM

growth rate.[40] However, this theory is still being improved so that it is directly applicable to these types of experiments.

In addition, the RT instability could be generated by making the Be thicker such that the flyer plate rarefaction catches up to the shock front before it crosses the Be/foam interface. This creates an unsteady blast wave that makes the interface RT unstable. As discussed by Drake, generating an RT instability is less difficult than an RM instability because a long lived steady shock is not required.[35] An experiment that generated both RM and RT is also easy to image. Early in time RM can dominate the perturbation growth and then later in time the RT instability can take over once the interface begins to decelerate.

Finally, the KH instability could also be generated with this platform. This platform is well suited for this instability because a pure KH instability requires a steady shear flow. In fact, the steady post-shock flow will generate supersonic shear flow, which can reduce the KH growth due to significant compressible effects. Due to the exponential dependence of the perturbation growth of both the RT and KH instabilities, it may be possible to observe a transition to turbulence with one of these instabilities.

3. TWO DIMENSIONAL SIMULATIONS

Two-dimensional (2D) ALEGRA simulations were performed in order to further evaluate the experimental design that was derived from 1D simulations.[41] The launching of the flyer plate in these simulations was driven by a temporal profile of the current that was previously produced by the Z machine. As already mentioned, this flyer plate geometry has been previously shot and has yielded reproducible results. However, for the simulations presented here the flight gap of the flyer was decreased from 4 mm to 1.5 mm to increase the planarity of the flyer at impact. Figure 3.1 below shows the initial setup of the simulation. At the perturbation the resolution is 12.5 μm in the amplitude direction and 25 μm along the wavelength direction. These simulations used the standard Steinberg-Guinan strength models and SESAME equations of states.

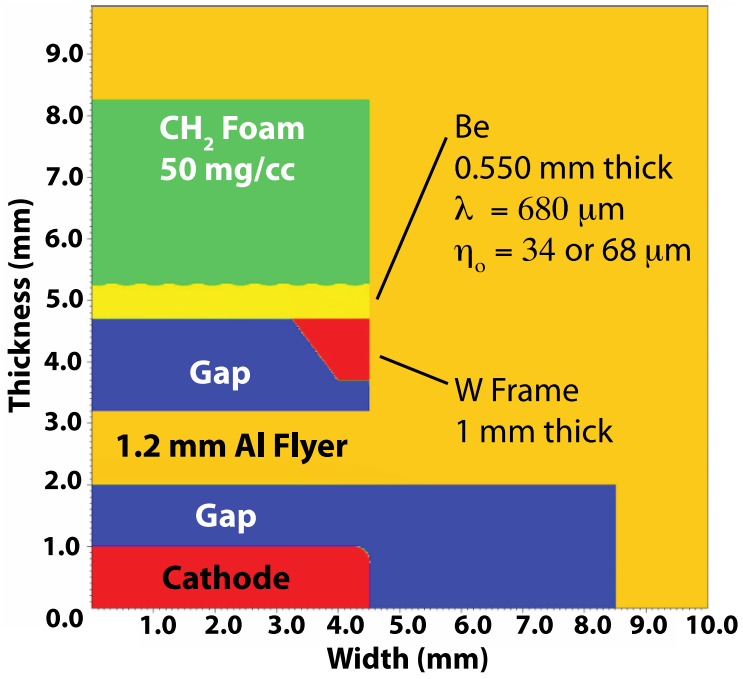

Figure 3.1. Shown here is the initial setup of the ALEGRA 2D simulations. The W frame is a Tungsten piece that is used to hold the target.

Figure 3.2 shows a time sequence of the entire simulation domain. In an actual experiment the backlighter x-rays will traverse the target from left to right. Thus, it is important that this line-of-sight remain clear of material that could possibly be launched from other parts of the target. So far these simulations show that the view of the perturbations remains unobstructed. Additional 2D simulations with a more accurate representation of the target geometry must be carried out to ensure remains true for the times of interest. Here the geometry was simplified in order to decrease the computational expense. It is important to note, that all previous 2D simulations of flyer plate driven targets modeled cross-sections taken through the vertical (z-axis) of the machine. This would be a plane containing the thickness and width of the target as defined in Figure 2.1. The simulations here are the same cross-section and thus cannot represent the actual

perturbation orientation. Here the simulations have used a perturbation wave vector that is rotated by 90 degrees. This does not affect usefulness of the simulations, since the perturbation wavelength is still much smaller than both dimensions of the flyer.

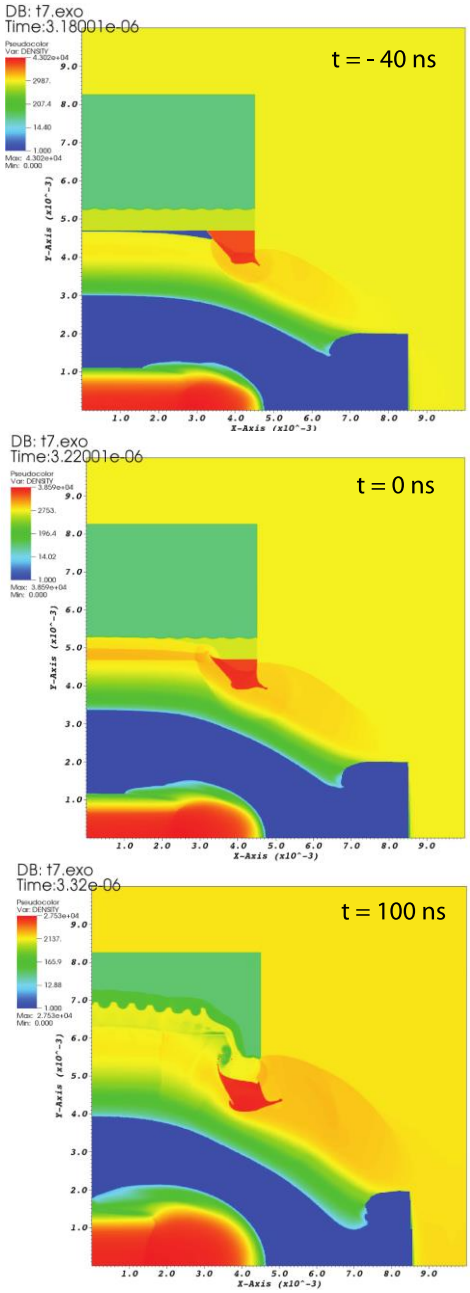

Figure 3.2. 2D ALEGRA simulations with an initial wavelength of 680 μm and a perturbation amplitude of 34 μm. The time t = 0 is defined as the time when the shock hits the perturbations.

Figure 3.3 shows magnified view of the perturbations for all three types of simulations. The 34 μm perturbation grows to ~200 μm (peak-to-valley), the 68 μm perturbation grows to ~300 μm (peak-to-valley), and the 68 μm perturbation, when no foam is present, grows to ~500 μm (peak-to-valley). The shock is visible in cases with foam, and as expected it is rippled after traversing the perturbation.

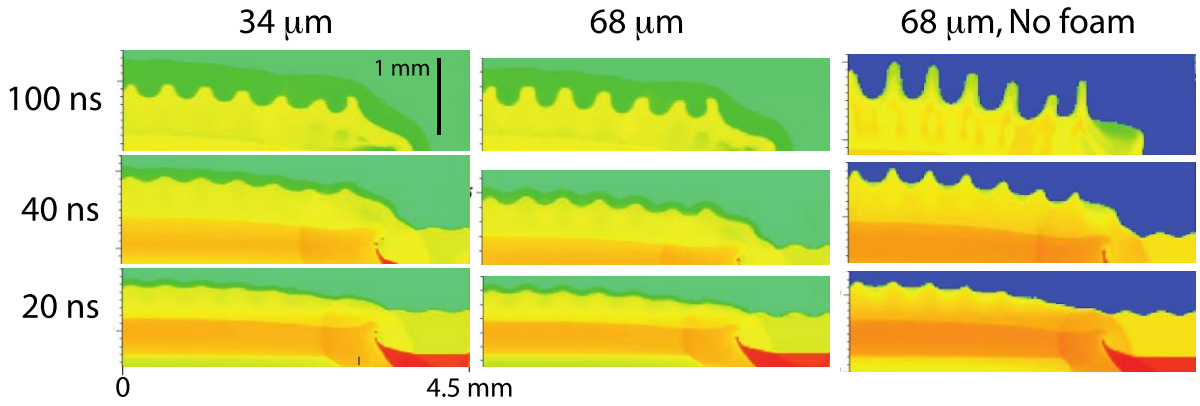

Figure 3.3. 2D ALEGRA simulations with 34 μm initial amplitude (left), 68 μm initial amplitude (center), and 68 μm amplitude with no foam. The width of the images in all cases is 4.5 mm, and the initial perturbation wavelength is 680 μm for all images. Again, t = 0 is defined as the time when the shock crosses the perturbed interface.

These simulations are encouraging, and lead us to believe that large RM spikes will be observable. If observed, these will be the largest RM spikes that have ever been created in the HED regime. Furthermore, these instabilities could be generated in the presence of an applied magnetic field. Recently, a 10 Telsa magnetic field was generated on Z using a pair of Helmholtz coils.[42] This capability has been developed to inject field into cylindrical liners before they implode. However, this capability could be used to embed a field into the planar targets designed here. It may then be possible to investigate the effects of the applied field on the growth of the RM instability, or perhaps other instabilities such as the Rayleigh–Taylor. A planar geometry may be relatively easy to diagnose compared to a cylindrical geometry .

4. CONCLUSIONS

This LDRD project sought to develop a new experimental platform for the Z machine in order to study hydrodynamic instabilities in high-energy-density plasma and warm dense matter. There are several instabilities that act in these systems, but this report focused on the Richtmyer-Meshkov (RM) instability. Because a detailed observation of this instability requires a long-lived steady shock, it has proved difficult to generate deep non-linear growth with laser driven targets. This report showed that the Z-machine is well suited for creating RM instabilities. Using an existing flyer plate configuration, the Be and foam target developed in this report can maintain a steady shock for 90 to 100 ns. This is enough time to grow a large RM instability that can be easily observed with the existing imaging diagnostic. Two-dimensional ALEGRA simulations confirmed that this experiment has the potential to create benchmark quality data. In the bigger picture, these types of instability experiments are necessary in order to improve our understanding of the basic mixing processes that occur in plasma flows. Both simulations and theory would benefit from a well-diagnosed mix experiment as proposed here. With minor changes, this platform could produce Rayleigh-Taylor and Kelvin-Helmholtz instabilities. Furthermore, Z could easily produce these instabilities in a semi-solid state where the growth rates are modified by the material's yield strength. Once the planar geometry is well understood, generating these instabilities in a cylindrically converging geometry may also be possible.

5. REFERENCES

1. M. E. Cuneo, M. C. Herrmann, D. B. Sinars, S. A. Slutz, W. A. Stygar, R. A. Vesey, A. B. Sefkow, G. A. Rochau, G. A. Chandler, J. E. Bailey, J. L. Porter, R. D. McBride, D. C. Rovang, D. C. Rovang, M. G. Mazarakis, E. P. Yu, D. C. Lamppa, K. J. Peterson, C. Nakhleh, S. B. Hansen, A. J. Lopez, M. E. Savage, C. A. Jennings, M. R. Martin, R. W. Lemke, B. W. Atherton, I. C. Smith, P. K. Rambo, M. Jones, M. R. Lopez, P. J. Christenson, M. A. Sweeney, B. Jones, L. A. McPherson, E. Harding, M. R. Gomez, P. F. Knapp, T. J. Awe, R. J. Leeper, C. L. Ruiz, G. W. Cooper, K. D. Hahn, J. McKenney, A. C. Owen, G. R. McKee, G. T. Leifeste, D. J. Ampleford, E. M. Waisman, A. Harvey-Thompson, R. J. Kaye, M. H. Hess, S. E. Rosenthal and M. K. Matzen, Ieee T Plasma Sci **40** (12), 3222-3245 (2012).
2. S. A. Slutz and R. A. Vesey, Phys Rev Lett **108** (2) (2012).
3. O. A. Hurricane, High Energ Dens Phys **4** (3-4), 97-102 (2008).
4. E. C. Harding, J. F. Hansen, O. A. Hurricane, R. P. Drake, H. F. Robey, C. C. Kuranz, B. A. Remington, M. J. Bono, M. J. Grosskopf and R. S. Gillespie, Phys Rev Lett **103** (4) (2009).
5. V. A. Smalyuk, J. F. Hansen, O. A. Hurricane, G. Langstaff, D. Martinez, H. S. Park, K. Raman, B. A. Remington, H. F. Robey, O. Schilling, R. Wallace, Y. Elbaz, A. Shimony, D. Shvarts, C. Di Stefano, R. P. Drake, D. Marion, C. M. Krauland and C. C. Kuranz, Phys. Plasmas **19** (9) (2012).
6. E. C. Harding, R. P. Drake, Y. Aglitskiy, T. Plewa, A. L. Velikovich, R. S. Gillespie, J. L. Weaver, A. Visco, M. J. Grosskopf and J. R. Ditmar, Phys. Plasmas **17** (5) (2010).
7. R. D. Richtmyer, Commun Pur Appl Math **13** (2), 297-319 (1960).
8. E. E. Meshkov, Fluid Dynamics **4** (5), 101 (1969).
9. A. L. Velikovich, Phys Fluids **8** (6), 1666-1679 (1996).
10. K. A. Meyer and P. J. Blewett, Phys Fluids **15** (3), 753-& (1972).
11. J. G. Wouchuk, Phys. Plasmas **8** (6), 2890-2907 (2001).
12. J. G. Wouchuk, Phys Rev E **63** (5) (2001).
13. G. M. Ward and D. I. Pullin, Phys Fluids **23** (7) (2011).
14. G. Dimonte and P. Ramaprabhu, Phys Fluids **22** (1) (2010).
15. A. L. Velikovich and G. Dimonte, Phys Rev Lett **76** (17), 3112-3115 (1996).
16. K. O. Mikaelian, Phys Rev Lett **80** (3), 508-511 (1998).
17. Q. Zhang and S. I. Sohn, Phys Lett A **212** (3), 149-155 (1996).
18. Q. Zhang and S. I. Sohn, Phys Fluids **9** (4), 1106-1124 (1997).
19. O. Sadot, L. Erez, U. Alon, D. Oron, L. A. Levin, G. Erez, G. Ben-Dor and D. Shvarts, Phys Rev Lett **80** (8), 1654-1657 (1998).
20. G. Malamud, C. A. Di Stefano, Y. Elbaz, C. M. Huntington, C. C. Kuranz, P. A. Keiter and R. P. Drake, High Energ Dens Phys **9**, 122 (2013).
21. G. Dimonte, C. E. Frerking, M. Schneider and B. Remington, Phys. Plasmas **3** (2), 614-630 (1996).
22. G. Dimonte and B. Remington, Phys Rev Lett **70** (12), 1806-1809 (1993).
23. R. L. Holmes, G. Dimonte, B. Fryxell, M. L. Gittings, J. W. Grove, M. Schneider, D. H. Sharp, A. L. Velikovich, R. P. Weaver and Q. Zhang, J Fluid Mech **389**, 55-79 (1999).

24. S. G. Glendinning, J. Bolstad, D. G. Braun, M. J. Edwards, W. W. Hsing, B. F. Lasinski, H. Louis, A. Miles, J. Moreno, T. A. Peyser, B. A. Remington, H. F. Robey, E. J. Turano, C. P. Verdon and Y. Zhou, Phys. Plasmas **10** (5), 1931-1936 (2003).
25. Y. Aglitskiy, N. Metzler, M. Karasik, V. Serlin, A. L. Velikovich, S. P. Obenschain, A. N. Mostovych, A. J. Schmitt, J. Weaver, J. H. Gardner and T. Walsh, Phys. Plasmas **13** (8) (2006).
26. Y. Aglitskiy, A. L. Velikovich, M. Karasik, N. Metzler, S. T. Zalesak, A. J. Schmitt, L. Phillips, J. H. Gardner, V. Serlin, J. L. Weaver and S. P. Obenschain, Philos T R Soc A **368** (1916), 1739-1768 (2010).
27. Y. Aglitskiy, M. Karasik, A. L. Velikovich, V. Serlin, J. L. Weaver, T. J. Kessler, S. P. Nikitin, A. J. Schmitt, S. P. Obenschain, N. Metzler and J. Oh, Phys. Plasmas **19** (10) (2012).
28. A. N. Aleshin, E. V. Lazareva, S. G. Zaitsev, V. B. Rozanov, E. G. Gamalii and I. G. Lebo, Dokl Akad Nauk Sssr+ **310** (5), 1105-1108 (1990).
29. J. W. Jacobs and V. V. Krivets, Phys Fluids **17** (3) (2005).
30. C. E. Niederhaus and J. W. Jacobs, J Fluid Mech **485**, 243-277 (2003).
31. J. F. Barnes, P. J. Blewett, R. G. McQueen, K. A. Meyer and D. Venable, J Appl Phys **45** (2), 727 (1973).
32. R. F. Benjamin and J. N. Fritz, Phys Fluids **30** (2), 331-336 (1987).
33. G. Dimonte, G. Terrones, F. J. Cherne, T. C. Germann, V. Dupont, K. Kadau, W. T. Buttler, D. M. Oro, C. Morris and D. L. Preston, Phys Rev Lett **107** (26) (2011).
34. W. T. Buttler, D. M. Oro, D. L. Preston, K. O. Mikaelian, F. J. Cherne, R. S. Hixson, F. G. Mariam, C. Morris, J. B. Stone, G. Terrones and D. Tupa, J Fluid Mech **703**, 60-84 (2012).
35. R. P. Drake, Phys. Plasmas **9** (8), 3545-3551 (2002).
36. D. B. Sinars, G. R. Bennett, D. F. Wenger, M. E. Cuneo, D. L. Hanson, J. L. Porter, R. G. Adams, P. K. Rambo, D. C. Rovang and I. C. Smith, Rev Sci Instrum **75** (10), 3672-3677 (2004).
37. D. B. Sinars, G. R. Bennett, D. F. Wenger, M. E. Cuneo and J. L. Porter, Appl Optics **42** (19), 4059-4071 (2003).
38. J. T. Larsen and S. M. Lane, J Quant Spectrosc Ra **51** (1-2), 179-186 (1994).
39. J. R. Robbins, (2013).
40. A. R. Piriz, J. J. L. Cela, N. A. Tahir and D. H. H. Hoffmann, Phys Rev E **78** (5) (2008).
41. A. C. Robinson, T. A. Brunner, S. Carroll, R. Drake, C. J. Garasi, H. Hanshaw, R. W. Lemke, E. Love, S. Mosso, J. Neiderhaus, C. Ober, S. Petney, W. J. Rider, G. Scovazzi, E. Strack, R. Summers, G. Weirs, M. Wong and T. Voth, 2008.
42. D. Rovang, (2013).

DISTRIBUTION

1	MS1189	Matt Martin	Org. 1641
1	MS1189	Dawn Flicker	Org. 1646
1	MS1193	Dan Sinars	Org. 1648
1	MS0899	Technical Library	9536 (electronic copy)

For LDRD reports, add:

1	MS0359	D. Chavez, LDRD Office	1911


Sandia National Laboratories